J Nanostruct 13(1): 159-172, Winter 2023

RESEARCH PAPER

Synthesis and Studying the Optical Properties of Novel Zinc Oxide/a symmetric dimer Liquid Crystal Nanohybrid

Zainab Rabeea Banoon *, Ali Kareem A. Al-Lami, Ahmed M. Abbas

Department of Chemistry, College of Science, University of Misan, Misan, Iraq

ARTICLE INFO

Article History:
Received 11 October 2022
Accepted 26 December 2022
Published 01 January 2023

Keywords:
Dimeric liquid crystal (Dimeric LCs)
Nanohybrid
Nanoparticles
Pl spectrum

ABSTRACT

In this work, a novel synthesis procedure was reported for the preparation of zinc oxide/liquid crystal nanohybrid. Also, the pure zinc oxide nanoparticles were synthesized through a hydrothermal route. Proton nuclear magnetic resonance (^{1}H- NMR), X-ray diffraction pattern (XRD), Fourier transform infrared (FTIR), scanning electron microscope (SEM), and transmission electron microscope (TEM) were used to analyze the structural and morphological characteristics of processed samples. The SEM images reveal that prepared zinc oxide has a uniform shape and size with an average of 58nm in diameter. It is found that the morphology of zinc oxide nanoparticles changes to cubic. The Nematic mesophases of Dimeric LCs were examined and described using a combination of two analytical methods: polarized optical microscopy (POM) and differential scanning calorimetry (DSC). Except for compound 5h, which forms SmA mesophases throughout a heating and cooling cycle, most compounds display Nematic mesophases. The optical properties of prepared liquid crystals were investigated via photoluminescence analysis in various solvents. The results showed that zinc oxide/liquid crystal nanohybrid has sufficient Pl spectrum that leads to the application of this nanohybrid in some optoelectronic applications such as cameras, medical devices, safety equipment and industrial equipment.

How to cite this article
Banoon Z R., Al-Lami A K., Abbas A M. Synthesis and Studying the Optical Properties of Novel Zinc Oxide/a symmetric dimer Liquid Crystal Nanohybrid. J Nanostruct, 2023; 13(1):159-172. DOI: 10.22052/JNS.2023.01.018

INTRODUCTION

In the recent ten years, there has been a lot of interest in the creation of liquid crystal materials (LCs), which are substances whose physical characteristics fall between those of normal liquids and those of solid crystals. This has been a subject of great interest in a variety of fields, including chemistry, physics, biology, telecommunications, and others, due to the significant achievements made in these areas [1, 2]. As model compounds for semi-flexible main-chain liquid crystal polymers, linear liquid crystal oligomers attracted interest. Dimeric liquid crystals exhibit significantly different mesosphere behavior than low molar mass liquid crystals [3-9]. Dimeric compounds are a class of liquid crystal compounds that have been widely studied in the literature. Researchers have focused on, for example, the synthesis of laterally connected dimers, rod- and disc-shaped systems, hydrogen-bonded dimers, light emitting dimers, cholesteryl-based dimers, thermotropic LCs-based-dimers, dimers containing triazole, non-symmetric dimers, flexible linear oligomers, and the twist-bend

* *Corresponding Author Email: zainabrabeea09@uomisan.edu.iq*

nematic phase [10-14]. However, the molecular engineering of compounds' architecture and functionalization significantly affect mesophase's physical properties like dielectric anisotropy, optical anisotropy, and thermal stability. The advancement of new technologies necessitated using smaller, more efficient, and greater power-density electrical equipment. To combat the heat created per unit volume, these clever electrical gadgets must properly drain the collected heat [15].

In recent years, using of metal oxide nanoparticles has found more attention [16-18]. These nanomaterials have thermal and chemical stability, large surface area, and excellent optical properties [19, 20]. Among metal oxide nanoparticles, zinc oxide nanoparticles showsuperior optical properties such as color absorption in the visible range and UV absorption [21, 22]. These nanoparticles have a wide range of applications, from catalysis and photocatalysis to drug delivery, environmental remediation, and electronics [23-25]. The structural and morphological features of produced ZnO nanoparticles determine the nanoparticles' ultimate properties [26-28]. The morphological and structural properties of zinc oxide nanoparticles were determined via synthesis route. Till now, various synthesis procedures was applied for preparation of zinc oxide nanoparticles [29-31]. Despite their potential benefits, metal oxide nanoparticles also present potential health and environmental risks [32-34]. The small size of these particles allows them to penetrate cells and tissues, potentially leading to toxicity and adverse health effects. Therefore, it is vital to understand and control the risks associated with metal oxide nanoparticle exposure to ensure their safe and sustainable use in various applications [35, 36]. The linking of metal oxide nanoparticles to organic compounds is an important ongoing research field in modern nanoscience and nanotechnology [37]. These materials benefit from the attractive features of both groups. Metal oxide nanoparticles/liquid crystals nanohybrids can act as response time elevator, with modified driving voltage and higher contrasts that are vital in the display industrial [38-40]. However, the synthesis of these nanoparticles has been faced with various challenges that limit their scale-up application. In this work, we introduce the novel nanohybrid zinc oxide nanoparticles/liquid crystals. The zinc oxide nanoparticles were prepared via a simple and novel chemical route. Several methods were used to characterize the produced samples, including FTIR, XRD, SEM, TEM, and PL analyses. Finally, a thorough characterization of the optical characteristics of the produced samples was performed.

MATERIALS AND METHODS

Materials

All reagents were purchased from commercial sources and used as received. P-hydroxybenzaldehyde from TCI, alkylbromides and 2-Amino-6-methoxybenzothiazole from sigma-Aldrich, p-hydroxyacetophenone, and Zinc chloride ($ZnCl_2.4H_2O$), and sodium hydroxide (NaOH) as precursors were purchased from Merck. Aluminum-backed silica-gel plates (Merk 60 F254) were used for the thin-layer chromatography (TLC) analysis, with examination under UV light. Also, all materials were applied in tests without further purification.

Characterizations

The IR spectra were recorded on a Bruker spectrometer as KBr pellets, and the ^{1}H NMR and ^{13}C NMR spectra were recorded on an ultra-shield 400 MHz Bruker FT-NMR spectrometer in CDCl3 and DMSO solution using tetramethylsilane (TMS) as an internal standard. Using a PerkinElmer Thermal Analyzer with a minimum heating rate, a differential scanning calorimeter (DSC) was used to analyze the transition temperatures and enthalpies. The thermal behavior and optical texture of several compounds were investigated using the Leica DM 2500P polarizing optical microscope (POM) equipped with an HCS302 heating stage. The crystalline structure was investigated via XRD patterns were obtained via Philips-X'pert pro-X-ray diffractometer using Ni-filtered Cu Kα radiation. LEO-1455VP instrument was applied for providing SEM analysis to study morphological properties. JEOL-2100F was used for providing TEM images for further morphological investigations. Shimadzu UV-2450 was applied for recording UV-DRS absorbance spectra and fluorescence spectra were recorded in a quartz cell (light path: 10 mm).

Synthesis of asymmetrical dimer liquid crystal

Williamson's ether synthetic reaction technique was used to create compound 1a-1h by reacting 4-hydroxybenzaldehyde with a range of (C1-C7,

C12) bromoalkane compounds [41]. By using the Claisen-Schmidt condensation process to combine 4-hydroxyacetophenone with compounds 1a-1h, chalcones (compounds 2a-2h) were created [42]. Through a condensation process between 2-Amimo-6-methoxybenzothiazole and 4-hydroxybenzaldehyde, compound 3 was created [43]. Williamson etherification of compound 2a-2h with 1,2-dibromoethane produced the intermediate compounds 4a-4h [44]. Similar

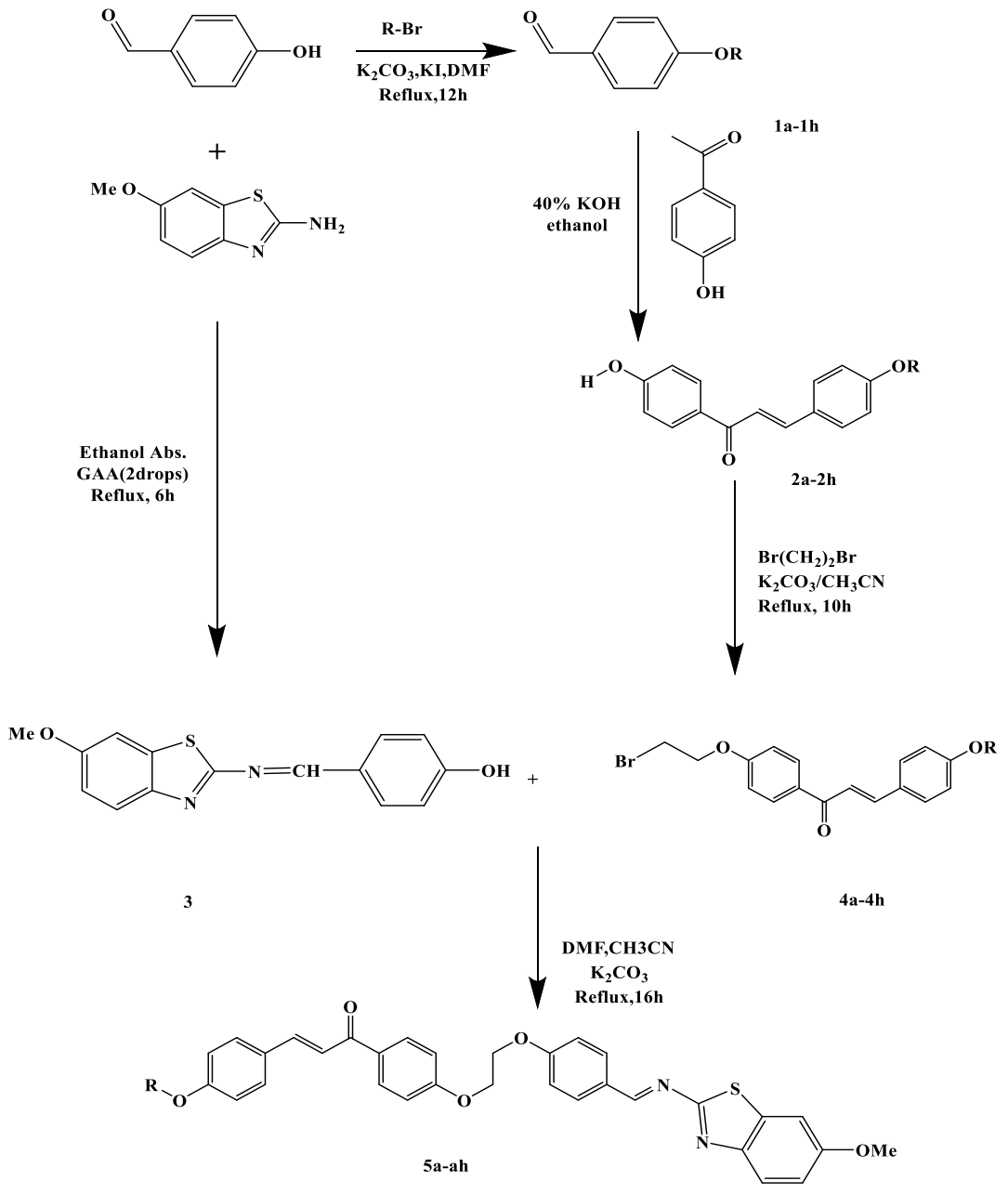

Series 5a-5h: 5a:R=CH_3 5b:R=C_2H_5 5c:R=C_3H_7 5d:R=C_4H_9 5e:R=C_5H_{11} 5f:R=C_6H_{13} 5g:R=C_7H_{15} 5h:R=$C_{12}H_{25}$

Fig. 1. Synthesis of targeted compounds 5a-5h, conditions, and pathways.

to how compounds 3 and other compounds 4a–4h were produced, compounds 5a–5h with minor modifications were likewise created using etherification condensation synthesis [45] (Fig. 1). Target compounds underwent FT-IR analysis, and ^{1}H and ^{13}C-NMR assignments were made. The measurements for the targeted substances are described and given information.

Synthesis of ZnO nanoparticles

0.3 g of $ZnCl_2.4H_2O$ was added to 25 mL of distilled water and stirred for 15 minutes. Then, PVP solution (0.1 g/mL) was added to a zinc-containing solution. The 2 M NaOH solution was added to the obtained solution drop by drop. The solution was changed to the milky phase and started to settled down. The mixture was transferred to a stainless autoclave and kept it at 140 ˚C for 8 h. Then, the white precipitate was separated via centrifuge at 12000 rpm for 15 min. The solid was washed three times with ethanol and deionized water. Finally, the product was dried overnight at 55 ˚C.

Liquid crystal / ZnO nanohybrid

The 0.05 g of prepared liquid crystal was dispersed in 25 mL of deionized water under mild stirring. After, 0.1 g of $ZnCl_2.4H_2O$ was solubilized in a liquid crystal mixture. The product was synthesized through a hydrothermal route (140 ˚C for 8 h). The as-obtained precipitate was separated via centrifuge at 6000 rpm for 15 min. The solid was washed with deionized water. Finally, the product was dried overnight at 55 ˚C.

General procedure for the synthesis of compounds (5a-5h)

6-Methoxy-2-(4-hydroxybenzylidenamino) benzothiazole (1.0 mmol), was dissolved in a minimum amount of DMF, then 30 mL of acetonitrile was added with potassium carbonate (2.0 mmol) was stirred for 1 h, and 1.0 mmol of appropriate compound 4a. The reaction mixture was refluxed at 76˚ C for 16 h. After completion of the reaction, the reaction system was poured into ice-cold water(120mL), and left with stirring until a yellow precipitate is obtained. The resulting precipitate was filtered off, washed and dried and purify via column chromatography on silica gel with a mixture of DCM / methanol =6: 0.05 (v/v) to obtain the compound's **5a-h** (85%-90%) yield.

The analytical data of FT-IR,^{1} H and ^{13}C NMR for title compounds 5a-h are summarised as follows:

5a. A greenish yellow solid; IR (Nujol) ν_{max} in cm^{-1}: 3039(C-H), 2927 and 2850(C-H aliphatic), 1674(C=O), 1651(CH=N), 1600(C=C Olifine), 1585-1419(C=C Ar), 1261(C-O). ^{1}H-NMR spectrum (400MHz, $CDCl_3$,ppm): 9.94(s,1H,CH=N), 8.12-8.06(d,2H,Ar-H), 7.93-7.87(d,2H, Ar-H), 7.85-7.80(d,1H, Olefinic H_β), 7.66-7.65(d,2H, Ar-H), 6.63-6.61(d,2H,Ar-H), 7.49-7.44(d,1H,OlefinicH_α), 7.13-7.04(m,7H,Ar-H), 4.48(s,4H,CH_2CH_2), 3.89(s,6H,OCH_3). ^{13}C-NMR(100MHz,CD Cl_3):55.45,66.41,66.63,114.40,114.43,114.92, 114 .97,119.46,127.76,130.18,130.39,130.77,131.91, 132.05,144.07,161.02,161.61,162.08,163.50,190. 80.

5b. A yellow solid; IR (Nujol) ν_{max} in cm^{-1}: 3039(C-H), 2974 and 2893(C-H aliphatic), 1689(C=O), 1651(CH=N), 1600(C=C Olifine), 1570-1423(C=C Ar), 1257(C-O). ^{1}H-NMR spectrum (400MHz, DMSO-d_6,ppm): 9.90(s,1H,CH=N), 8.20-8.17(d,2H,Ar-H), 7.93-7.90(d,2H, Ar-H), 7.89-7.86(d,1H, Olefinic H_β), 7.84-7.81(d,4H, Ar-H), 7.72-7.67(d,1H,OlefinicH_α),7.24-7.00(m,7H,Ar-H),4.50(s,4H,CH_2CH_2),4.14-4.07(q,2H,OCH_2) 3.44(s,3H,OCH_3),1.38-1.34(t,3H,CH_3). ^{13}C-NMR(100MHz,DMSO-d_6):15.03,55.82,63.81 ,67.0 0,67.22114.41,114.97,115.26,115.51,119.83,127. 76,130.33,131.20,131.31,131.40,132.34,143.75,1 61.02,162.54,163.71,191.87.

5c. A yellow solid; IR (Nujol) ν_{max} in cm^{-1}: 3070(C-H),2954 and 2866(C-H aliphatic), 1689(C=O),1651(CH=N),1600(C=C Olifine), 1570-1423(C=C Ar), 1253(C-O). ^{1}H-NMR sp ectrum(400MHz,$CDCl_3$,ppm):9.94(s,1H,CH =N),8.11-8.08(d,2H,Ar-H),7.92-7.91(d,2H,Ar-H),7.85-7.61(d,1H,OlefinicH_β),7.50-7.45(d,1H,OlefinicH_α),7.11-6.94(m,7H,Ar-H),4.48(s,4H,CH_2CH_2),4.06(t,2H,OCH_2),3.89(s,3H ,OCH_3), 1.53(m,2H,CH_2),1.05-0.92(t,3H,CH_3).^{13}C-NMR(100MHz,$CDCl_3$):14.16,22.73,55.82, 66.40,6 6.50,66.63,114.39,114.41,114.92,115.96,119.25, 127.52,130.18,130.38,130.76,131.94,132.05,144 .16,144.20,161.24,161.25,162.06,162.14,163.50 ,190.81.

5d. A greenish yellow solid; IR (Nujol) ν_{max} in cm^{-1}: 3062(C-H), 2954 and 2870(C-H aliphatic), 1685(C=O), 1651(CH=N), 1600(C=C Olifine), 1570-1423(C=C Ar), 1253(C-O). ^{1}H-NMR spectrum (400MHz,$CDCl_3$,ppm): 9.90(s,1H,CH=N), 8.20-8.16(d,2H,Ar-H), 7.93-7.91(d,2H, Ar-H), 7.90-7.89(d,1H, Olefinic H_β), 7.86-7.81(d,4H, Ar-H), 7.72-7.69(d,1H, Olefinic H_α), 7.24-7.00(m,7H,

Ar-H), 4.44(s,4H,CH_2CH_2), 4.02-3.99(t,2H,OCH_2) 3.80(s,3H,OCH_3), 1.80-1.76(q,2H,CH_2) 1.47-1.41(q,2H,OCH_2), 1.00-0.96(t,3H,CH_3).^{13}C-NMR(100MHz,$CDCl_3$): 13.87,19.25,31.96,55.41,66.39,66.50,66.63,114.10,114.39114.92,115.96,119.25,119.29,123.50,127.52,127.51,130.18,130.38,130.77,131.94,139.31,144.19,144.23,161.24,161.26,162.06,162.13,163.50,190.81.

5e. A greenish yellow solid; IR (Nujol) ν_{max} in cm^{-1}: 3070(C-H), 2931 and 2854(C-H aliphatic), 1689(C=O), 1651(CH=N), 1600(C=C Olifine), 1566-1423(C=C Ar), 1253(C-O). ^{1}H-NMR spectrum (400MHz,DMSO-d_6,ppm): 9.91(s,1H,CH=N), 8.21-8.17(d,2H,Ar-H), 7.93-7.90(d,2H, Ar-H), 7.89-7.87(d,1H, Olefinic H_β), 7.84-7.82(d,4H, Ar-H), 7.73-7.67(d,1H, Olefinic H_α), 7.24-6.94(m,7H, Ar-H), 4.51(s,4H,CH_2CH_2), 4.07-4.03(t,2H,OCH_2) 3.41(s,3H,OCH_3), 1.77-1.70(q,2H,CH_2) 1.43-1.21(m,4H,$2CH_2$), 0.94-0.90(t,3H,CH_3).^{13}C-NMR(100MHz,DMSO,d_6): 14.41,22.37,28.16, 28.78,55.81,67.00,67.23,68.15,114.41,114.97,115.29,115.52,119.82,127.77,130.34,131.19,131.31,131.41,139.34,143.44,143.74,161.02-,161.16,162.54,163.72,191.85.

5f. A yellow solid; IR (Nujol) ν_{max} in cm^{-1}: 3074(C-H), 2935 and 2866(C-H aliphatic), 1689(C=O), 1651(CH=N), 1600(C=C Olifine), 1566-1423(C=C Ar), 1257(C-O). ^{1}H-NMR spectrum (400MHz,DMSO-d_6,ppm): 9.91(s,1H,CH=N), 8.20-8.18(d,2H,Ar-H), 7.94-7.92(d,2H, Ar-H), 7.91-7.90(d,1H, Olefinic H_β), 7.87-7.82(d,4H, Ar-H), 7.73-7.68(d,1H, Olefinic H_α), 7.24-7.01(m,7H, Ar-H), 4.51(s,4H,CH_2CH_2), 4.07-4.03(t,2H,OCH_2) 3.39(s,3H,OCH_3),1.79-1.70(q,2H,CH_2) 1.46-1.25(m,6H,$3CH_2$), 0.92-0.88(t,3H,CH_3).^{13}C-NMR(100MHz,DMSO-d_6): 14.40,22.56,25.64,29.06,31.48,55.45,67.01,67.23, 68.17,114.97,115.29,115.52,119.82,127.77,130.35,131.19,131.30,131.42,132.34,143.75,161.02,161.19,162.54,163.72,191.85.

5g. A greenish yellow solid; IR (Nujol) ν_{max} in cm^{-1}: 3070(C-H), 2935 and 2850(C-H aliphatic), 1689(C=O), 1651(CH=N), 1600(C=C Olifine), 1566-1423(C=C Ar), 1253(C-O). ^{1}H-NMR spectrum (400MHz,$CDCl_3$,ppm): 9.82(s,1H,CH=N), 7.98-7.95(d,2H,Ar-H), 7.79-7.73(d,2H, Ar-H), 7.70-7.68(d,1H, Olefinic H_β), 7.52-7.44(d,4H, Ar-H), 7.37-7.31(d,1H, Olefinic H_α), 7.00-6.85(m,7H, Ar-H), 4.36(s,4H,CH_2CH_2), 3.93-3.91(t,2H,OCH_2) 3.40(s,3H,OCH_3), 1.74-1.70(q,2H,CH_2) 1.34-1.29(q,2H,CH_2), 1.26-1.17(m,6H,$3CH_2$),0.84-0.82(t,3H,CH_3).^{13}C-NMR(100MHz,$CDCl_3$): 14.16,22.73,26.00,28.94,29.11,31.96,55.81,66.40,66.63,68.22,114.10,114.39,114.89.115.96,119.24,119.26,123.50,127.50,127.51,130.18,130.38,130.77,131.93,139.30,144.19,144.22,161.24,161.27,162.07,162.13,163.51,190.80.

5h. A yellow solid; IR (Nujol) ν_{max} in cm^{-1}: 3070(C-H), 2916 and 2850(C-H aliphatic), 1689(C=O), 1651(CH=N), 1600(C=C Olifine), 1573-1423(C=C Ar), 1257(C-O). ^{1}H-NMR spectrum (400MHz,DMSO-d_6,ppm): 9.91(s,1H,CH=N), 8.20-8.18(d,2H,Ar-H), 7.94-7.91(d,2H, Ar-H), 7.90-7.87(d,1H, Olefinic H_β), 7.84-7.82(d,4H, Ar-H), 7.73-7.68(d,1H, Olefinic H_α), 7.24-7.01(m,7H, Ar-H), 4.51(s,4H,CH_2CH_2), 4.07-4.03(t,2H,OCH_2) 3.39(s,3H,OCH_3), 1.74-1.70(q,2H,CH_2) 1.46-1.41(q,2H,CH_2), 1.39-1.29(m,16H,$8CH_2$),0.94-0.90(t,3H,CH_3).^{13}C-NMR(100MHz,DMSO-d_6): 14.13,22.76,26.31,29.38,29.40,29.52,29.56,29.62,29.66,29.71,31.64,55.81,68.04,67.93,67.83,114.10,114.39,114.92.115.96,119.24,119.26,123.50,127.50,127.51,130.18,130.38,130.74,131.93,139.30,144.19,144.22,161.24,161.27,162.05,162.13,163.51,191.56.

RESULTS AND DISCUSSION

FT-IR, NMR spectral studies

In the FTIR spectrum of compound 5a (Fig. 2a). The absorption in the region 3039 cm^{-1} refers to the C-H (sp^2) stretching, while the bands at 2916 and 2839 cm^{-1} are assigned for the symmetrical and asymmetrical C-H (sp^3) stretching and the carbonyl group also shifted 1674 cm^{-1}characteristic for conjugated carbonyl vibration [46]. The C=N bond of the Schiff base can be used to explain the band with a strong intensity seen at 1651 cm^{-1}. This absorption band crossed across with the band originating from the benzothiazole ring's C=N, creating a distinct and potent absorption band [47]. The product also showed absorption peaks at 1600 cm^{-1} (C=C Olifinic) and a very strong band occurred at 1261 cm^{-1} can be ascribed to the stretching of the ether (C–O–C) bond. Fig. 2b shows the FTIR spectrum of the prepared ZnO/liquid crystal nanohybrid. As well as shown, the peak at 520 cm^{-1} is attributed to the Zn-O bond in nanohybrid. The liquid crystal-related FTIR peaks are observable in the FTIR spectrum of nanohybrid (Fig. 2b).

In the ^{1}H-NMR spectrum of compound 5a will be used as an example (Fig.3), the singlet observed at the most downfield region, δ=9.94 ppm, supported the presence of the imine linking group[48]. Fifteen aromatic protons are observed

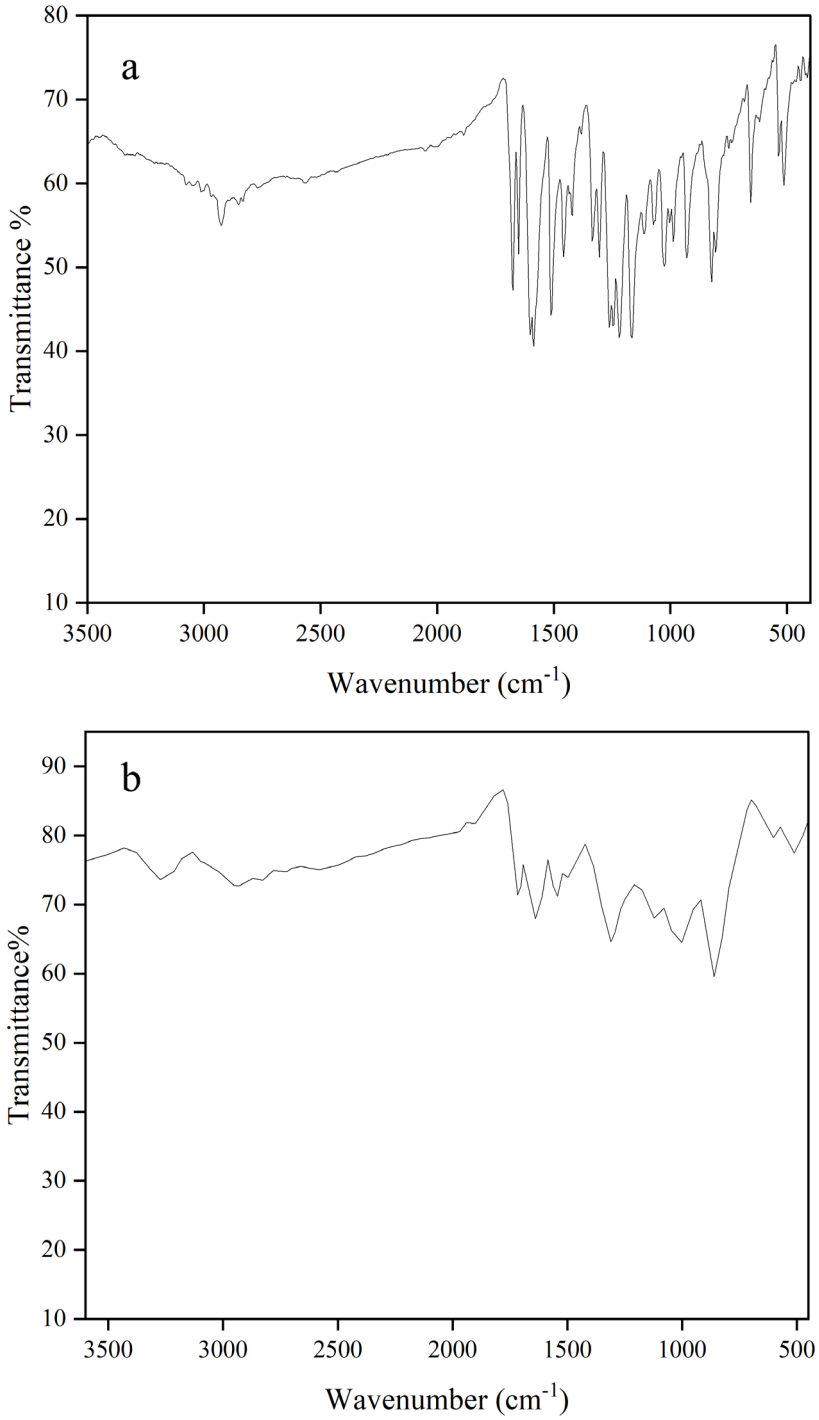

Fig. 2. FTIR spectra of prepared a) compound 5a b) zinc oxide/liquid crystal nanohybrid

within the chemical shift range of δ=8.12-6.95ppm. The Olefinic protons showa characteristic doublet at δ=7.85,7.80,7.49 and 7.44ppm respectively, singlet at δ=3.89 ppm to the methyl protons that directly connected to an oxygen atom (-OCH_3). Another methylene proton (-O-CH_2CH_2-O-) gave a

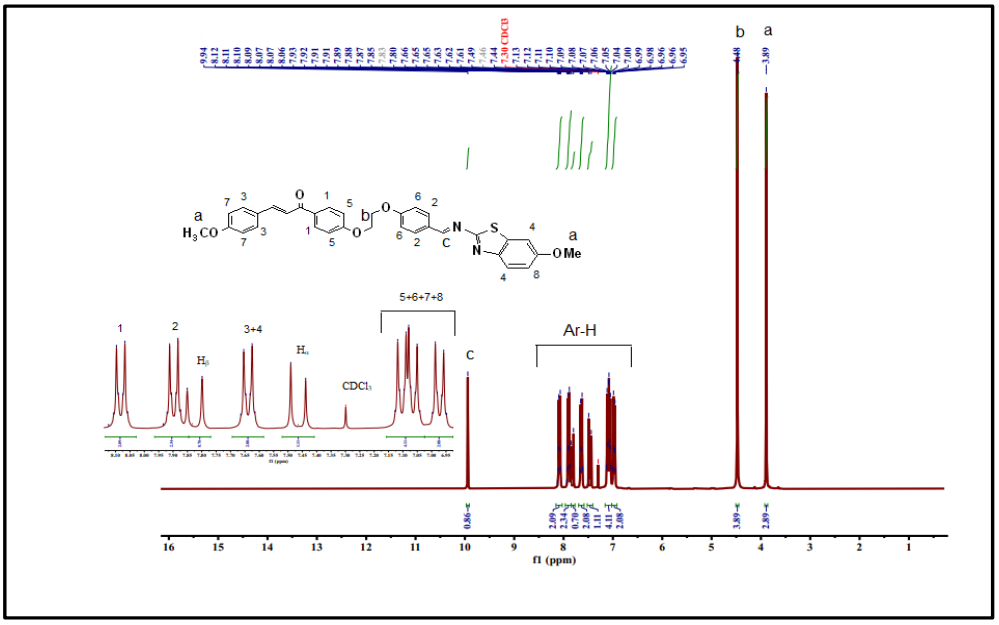

Fig. 3.^{1}H (400 MHz, $CDCl_3$) NMR spectrum of compound 5a.

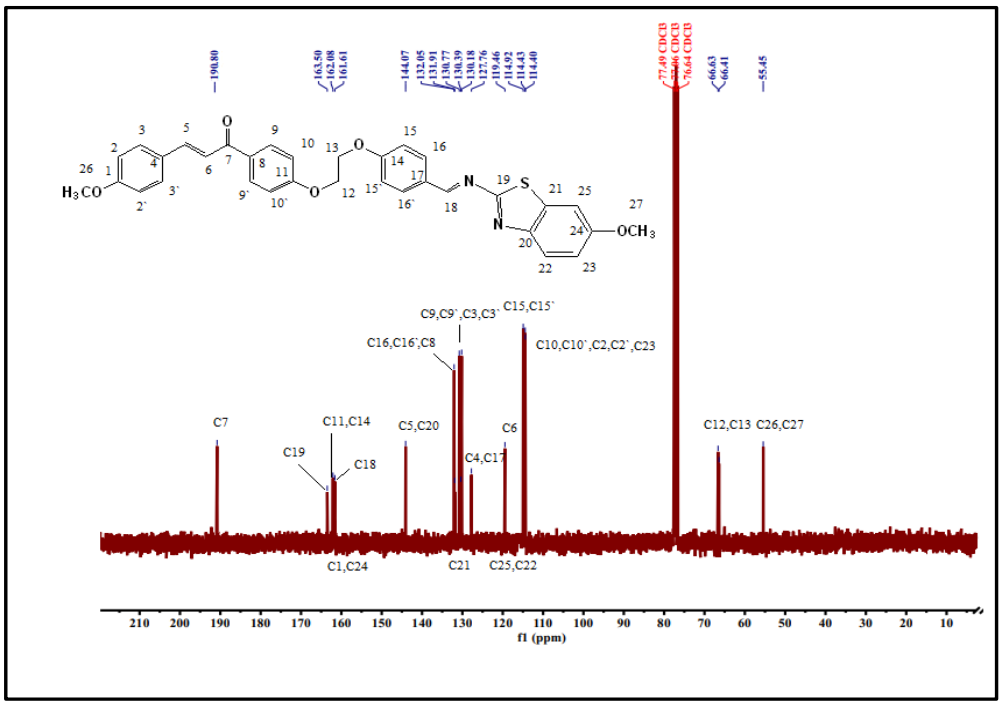

Fig. 4.^{13}C-NMR (100 MHz, $CDCl_3$) spectrum of compound 5a.

singlet signal at δ=4.48ppm.

The ^{13}C-NMR spectrum (Fig. 4) of compound 5a showed the presence of 27 carbons-two methyl, two methylene, eleven aromatic, eleven

Table 1. DSC findings summarizing the phase temperatures and enthalpy changes of compounds 5a-5h.

No	sold- sold (˚C)	Transition (˚C)	ΔH KJ/mole	ΔS J/mole.K	ΔT_N (˚C)	ΔT_S (˚C)
5a	-	C→N 148 .72 N→I 153.33	111.586	264.50	4.61	-
5b	-	C→N 143.92 N→I 150.73	18.654	44.72	6.81	-
5c	-	C→N 113.09 N→I 172.42	23.882 10.821	61.832 24.285	59.33	-
5d	79.91	C→N 107.35 N→I 182.37	9.801	25.758	75.02	-
5e	-	C→N 126.13 N→I 150.04	57.851	144.888	23.91	-
5f	-	C→N 128.28 N→I 179.06	33.789	84.171	50.78	-
5g	-	C→N 108.07 N→I 117.44	35.086	92.036	9.37	-
5h	-	C→S_A 101.43 S_A →N 122.80 N→I 157.04	13.429 8.324 16.835	35.850 21.022 39.133	34.24	21.37

Note: C=Crystal, SmA= smectic A phase, I= Isotropic phase, N= nematic phase.

quaternary and one azomethine carbons.

Phase transition and mesomorphic behaviour in compounds 5a-5h

According to the method described in the literature, the desired non-symmetric dimeric liquid crystalline molecules have been produced. The synthesis approach is shown in Fig. 1. The phase transition temperatures and mesomorphic properties were investigated using a powder X-ray

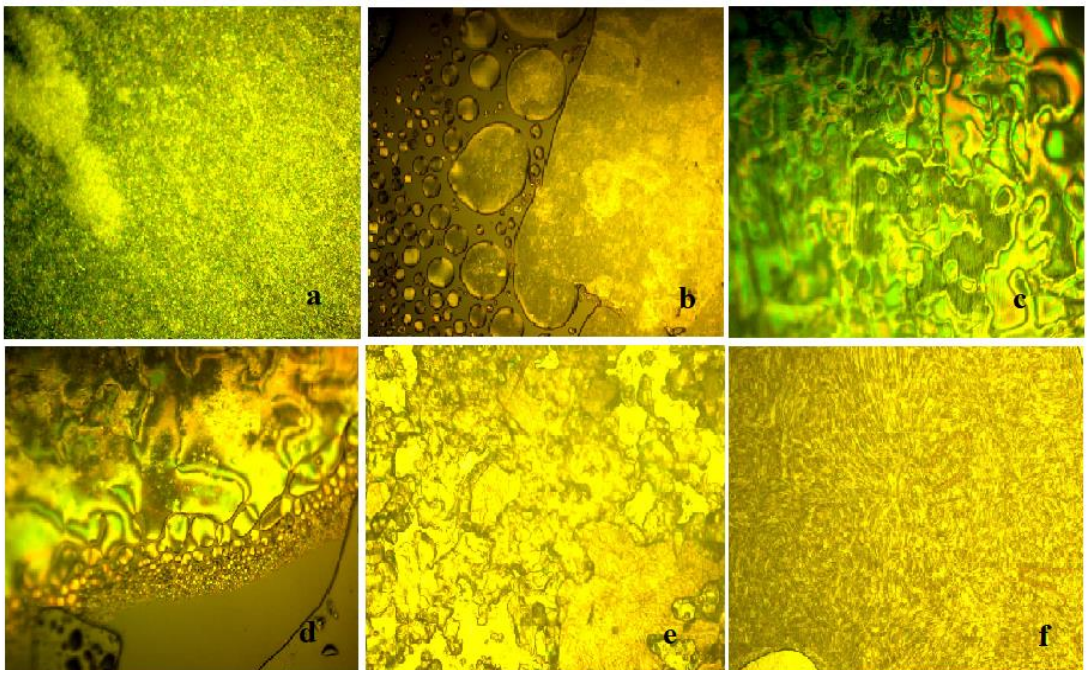

Fig. 5. POM images (a) compound 5a, (b) compound 5c, (c) compound 5e, (d) compound 5f, (e) compound 5g, and (f) compound 5h.

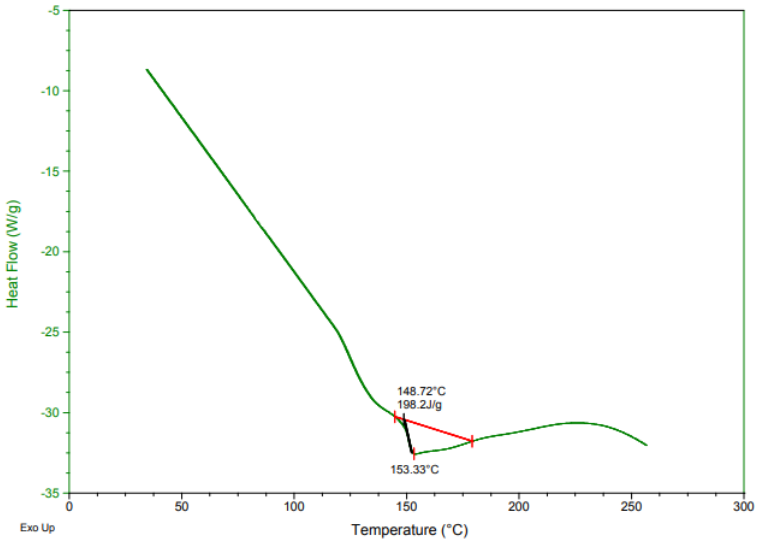

Fig. 6 DSC curve of compound 5a during heating scans.

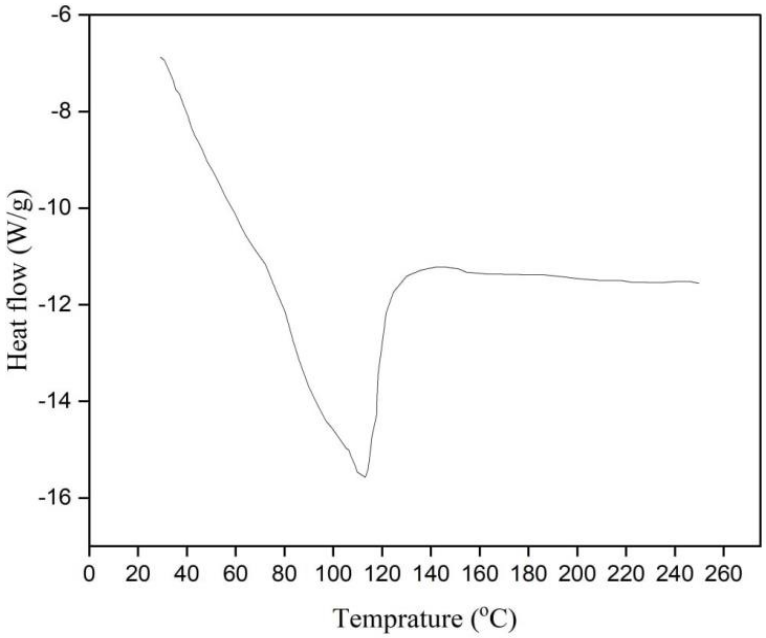

Fig. 7 DSC curve of LCs nanocomposites during heating scans.

diffractometer (XRD), polarized optical microscopy (POM), and differential scanning calorimetry (DSC). Related enthalpy shifts and phase behavior as a function of temperature are displayed in Table 1. Liquid crystal characteristics may be seen in the targeted compounds 5a–5.

Textures such as the nematic phase, Droplet, Schlieren, Thread-like, and Marble, are seen in Fig. 5. Compound 5a displays nematic behavior. DSC experiment heating scans revealed a Cr phase at 148.72°C (ΔH = 111.586), with the transition state as Cr -N-Iso. The following heating shows the Cr-N transition and the mesophase region at 4.61°C. As of 153.33°C, the liquid begins to clarify. In a thermal

scan, POM showed a texture similar to thread. Heat alters the texture of Nematic, as shown in Fig. 5a, from the DSC experiment, Fig. 6. When compound 5b is heated, the same thing happens to it. The DSC thermogram further verifies that the liquid crystalline phase has formed in compound 5b.

The DSC thermogram showed the onset of the crystal phase at 143.92 °C (ΔH=18.65), and the isotropic transition temperature was located at 150.73 °C. Interestingly, the emergence of the nematic phase was confirmed by optical microscope observation following heating and cooling cycles of 5c-5h compounds. Compound 5c, for instance, exhibits a transition on the heating scan between the Cr-N-Iso phases at 113.09 °C (ΔH= 23.88) and 172.42 °C(ΔH= 10.82). Compound 5c was observed under an optical microscope, and cooling scans revealed that the droplet nematic phase had changed into the Thread-like texture (Fig. 5b). Similar results were seen with compounds 5d-5g. Fig. 5 (c), (d), and (e) show the POM textures of compounds 5e, 5f, and 5g after several chilling cycles.

The DSC thermogram further verifies that component 5h has entered the liquid crystalline phase (Fig. 6). Cr-SmA-N-Iso transitions were detected during the scanning of compound 5h. The crystallization transition from Sm to SmA occurs at 101.43 °C (ΔH = 13.429), the Sm to N transition is confirmed at 122.80 °C (ΔH = 8.324), and the N to Iso transition is confirmed at 157.04 °C (ΔH = 16.835). POM scans taken after cooling revealed the threadlike texture. The texture of cooled Nematic is seen in Fig. 5f.

DSC analysis was also used to investigate the thermal characteristics of LCs-nanocomposites. The composites' dynamic scan is depicted at 10 °C/min in Fig. 7. The crystalline phases were clearly changed to lower temperatures by adding ZnO nanoparticles. By filling the gaps between molecules, the addition of ZnO and nanoparticles decreased the free volume inside the composites. As a result, the LCs' mobility is decreased. Additionally, nanoparticles function as crystallization nucleation sites. As a result, the

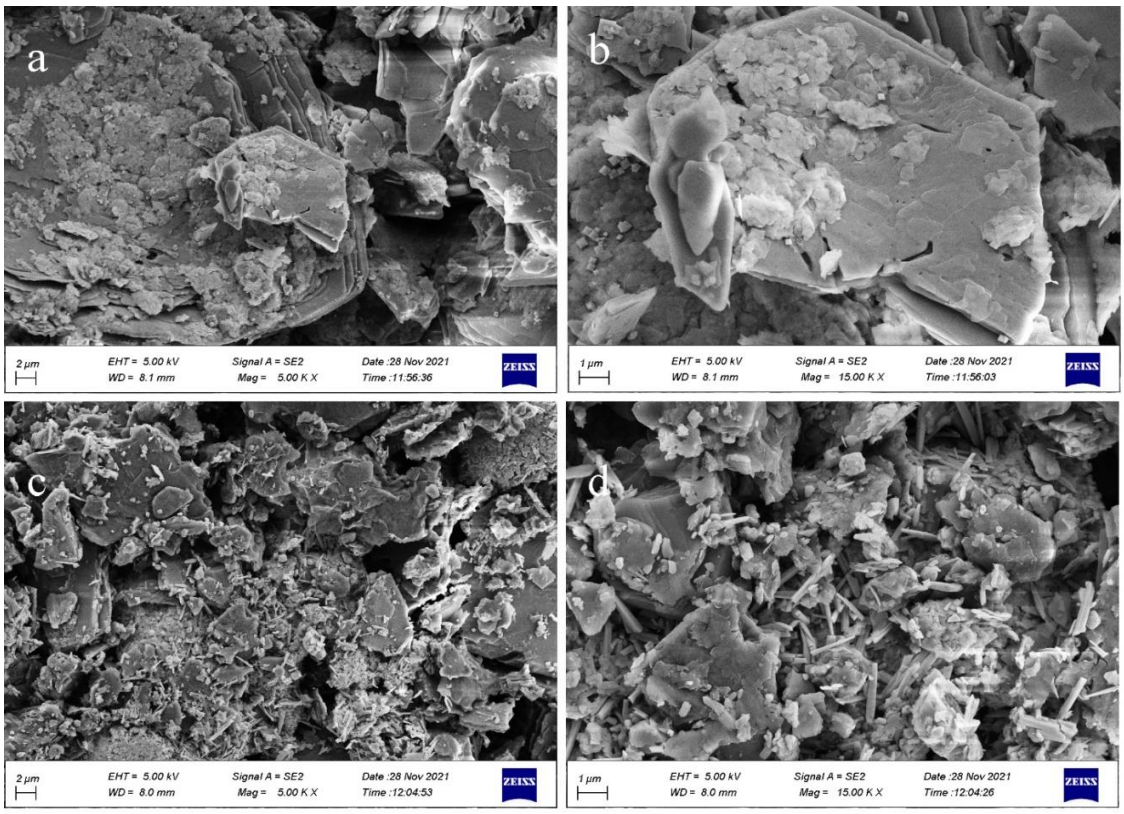

Fig. 8. SEM images of a,b) zinc oxide nanoparticles (c,d) zinc oxide/liquid crystal nanohybrid.

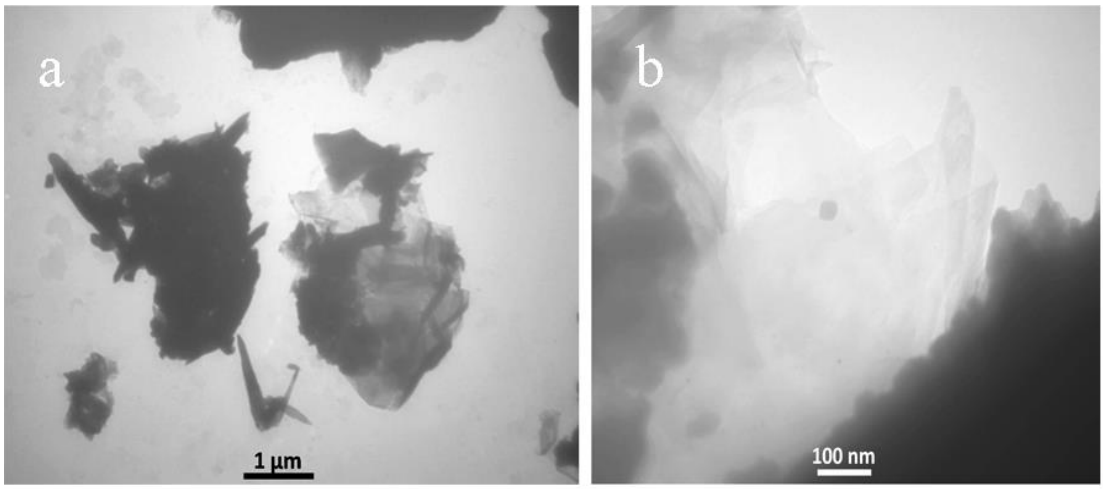

Fig. 9. TEM images of prepared zinc oxide/liquid crystal nanohybrid.

creation of a network of nanoparticles lowers the overall mobility of composites. This was consistent with the earlier finding that nematic liquid crystals' phase transition temperature decreases when graphene oxide (GO) is added [49].

The morphology and structure of LCs and LC-nanocomposites

The shape and size of prepared nanoparticles were characterized via SEM and TEM analysis. Fig. 8a and Fig. 8b present the scanning electron microscopy images (SEM) of as-obtained zinc oxide nanoparticles. The SEM images reveals that prepared zinc oxide has a uniform shape and size with an average of 58 nm in diameter. Fig. 8c and Fig. 8d present the SEM image of the prepared zinc oxide/liquid crystal nanohybrid. It is found that the morphology of zinc oxide nanoparticles changes to cubic. This can be related to the effect of liquid crystals that link on the surface of nanoparticles and control the morphology and size of particles. The composite materials' performance was boosted by the incorporation of uniformly dispersed inorganic nanoparticles [50]. TEM images of prepared nanohybrid are presented in Fig. 9a and Fig. 9b. It can be seen that the TEM images confirm the formation of uniform zinc oxide nanoparticles in agreement with SEM results.

XRD patterns were used for tracking the phase formation and crystal structure of prepared zinc oxide nanoparticles. Fig. 10 shows the X-ray diffraction pattern of prepared ZnO nanoparticles. As shown, (100), (1002), (101), (102), (110), (103), and (112) planes are compatible with JCPDS No. 01-080-0075. On the other side, the mean crystal sizes (L) for ZnO nanoparticles were calculated by utilizing Scherer's equations[51, 52].

$$L = \frac{k\,\lambda}{\beta\,Cos\,\theta} \quad (1)$$

Where k = 0.9 is the constant crystal lattice, λ,β and θ are indicated to shape constant, the wavelength of the radiation, Bragg diffraction angle, and full width at half maximum intensity (FWHM).

The result indicates that it has a nano-size equal to 19.8 nm.

The FTIR, DSC, POM, SEM, TEM and XRD analysis revealed that the applied synthesis route prepared zinc oxide/liquid crystal nanohybrid successfully.

Photoluminescence (PL) study

The absorbance and PL spectra of the prepared compounds were recorded in methanol as a solvent, at a wavelength λ = 250–700 nm. The spectra of representative compounds 5a and as-obtained zinc oxide/liquid crystal nanohybrid are shown in Fig. 11 (a) and (b) which were selected as an example because the PL spectra of compounds 5a–5h are analogous. However, the varied terminal alkyl chain length has an insignificant influence on their emission bands [53]. As well as observable, the emission appears in the blue region located at λ_{max} = 380 nm. These emission bands can be attributed to π–π* electronic transition involving

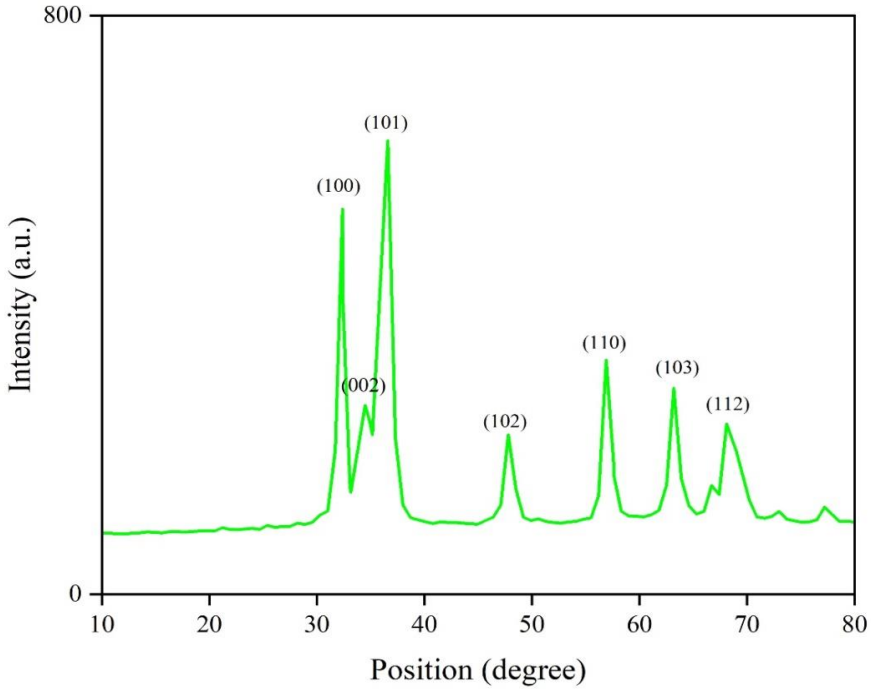

Fig. 10. XRD pattern of prepared zinc oxide nanoparticles.

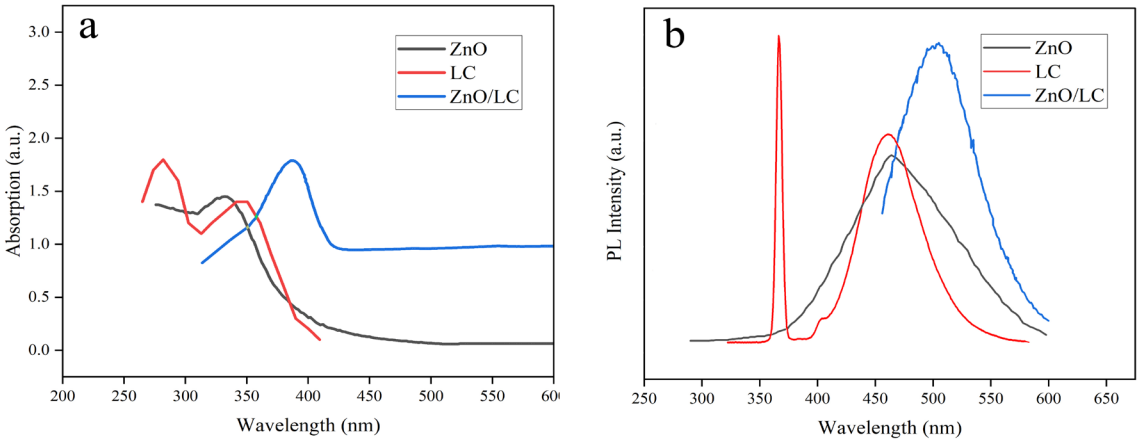

Fig. 11. a) Uv-vis absorption spectra. b) Fluorescence spectra in methanol solvent.

the whole electronic system of the compound. Fig. 11b shows the Pl analysis of the as-obtained zinc oxide/liquid crystal nanohybrid. As well as shown, the introduction of ZnO nanoparticle reduces the intensity of Pl slightly, but does not quench it. Also, this confirms the attached liquid crystal on the surface of zinc oxide nanoparticles. It can be concluded that prepared zinc oxide/liquid crystal nanohybrid can be applied in the optoelectronic field successfully. The material features blue light emission capabilities that might be used in applications including OLED materials, fluorescent probes for biological applications, and biotags for biological sensing applications, as shown by the

emission in the blue region λ = 420–500 nm [54, 55].

CONCLUSION

In conclusion, the synthesis and characterization of novel nonsymmetrical Dimeric compounds, combined with the use of liquid crystal and zinc oxide nanoparticles, have been successfully demonstrated. The comprehensive analysis of the prepared products using XRD, FTIR, SEM, TEM, and PL techniques provided significant insights into the structure and properties of the materials. The SEM and TEM images confirmed the formation of pure zinc oxide nanoparticles, while the successful linking of the liquid crystal to the surface of the zinc oxide nanoparticles was demonstrated. Furthermore, the PL analysis suggested that the resulting zinc oxide/ liquid crystal nanohybrid could have great potential in optoelectronic fields. Overall, this study presents a promising direction for the development of new materials with interesting properties for various technological applications.

CONFLICT OF INTEREST

The authors declare that there is no conflict of interests regarding the publication of this manuscript.

REFERENCES

1. Prakash J, Khan S, Chauhan S, Biradar AM. Metal oxide-nanoparticles and liquid crystal composites: A review of recent progress. J Mol Liq. 2020;297:112052.
2. Patro CK, Verma R, Garg A, Dhar R, Dabrowski R. Boost in the thermal stability, ionic conductivity and director relaxation frequency in the composite of liquid crystal and functionalised multi-walled carbon nanotubes. Liq Cryst. 2020;48(3):345-360.
3. Imrie CT. Non-symmetric liquid crystal dimers: how to make molecules intercalate. Liq Cryst. 2006;33(11-12):1449-1485.
4. Abberley JP, Killah R, Walker R, Storey JMD, Imrie CT, Salamończyk M, et al. Heliconical smectic phases formed by achiral molecules. Nature Communications. 2018;9(1).
5. Salamończyk M, Vaupotič N, Pociecha D, Walker R, Storey JMD, Imrie CT, et al. Multi-level chirality in liquid crystals formed by achiral molecules. Nature Communications. 2019;10(1).
6. Walker R, Majewska M, Pociecha D, Makal A, Storey JMD, Gorecka E, et al. Twist-Bend Nematic Glasses: The Synthesis and Characterisation of Pyrene-based Nonsymmetric Dimers. Chemphyschem. 2021;22(5):461-470.
7. Walker R, Pociecha D, Storey JMD, Gorecka E, Imrie CT. The Chiral Twist-Bend Nematic Phase (N* TB). Chemistry – A European Journal. 2019;25(58):13329-13335.
8. Walker R, Pociecha D, Abberley JP, Martinez-Felipe A, Paterson DA, Forsyth E, et al. Spontaneous chirality through mixing achiral components: a twist-bend nematic phase driven by hydrogen-bonding between unlike components. Chem Commun. 2018;54(27):3383-3386.
9. Walker R, Pociecha D, Strachan GJ, Storey JMD, Gorecka E, Imrie CT. Molecular curvature, specific intermolecular interactions and the twist-bend nematic phase: the synthesis and characterisation of the 1-(4-cyanobiphenyl-4′-yl)-6-(4-alkylanilinebenzylidene-4′-oxy)hexanes (CB6O.m). Soft Matter. 2019;15(15):3188-3197.
10. Umadevi S, Sadashiva BK. Liquid crystalline properties and dependence of transition temperatures on the length of the flexible alkylene spacer of symmetric dimers composed of bent-core units. Liq Cryst. 2007;34(6):673-681.
11. Zhang C, Jin L, Yin B, Jamil M, Jeon YJ. Synthesis and properties of non-symmetric liquid crystal dimers containing a cholesteryl moiety. Liq Cryst. 2008;35(1):39-44.
12. Al-Lami AK. Preparation and Mesomorphic Characterization of Supramolecular Hydrogen-Bonded Dimer Liquid Crystals. Polycyclic Aromatic Compounds. 2015;36(3):197-212.
13. Tuchband MR, Paterson DA, Salamończyk M, Norman VA, Scarbrough AN, Forsyth E, et al. Distinct differences in the nanoscale behaviors of the twist–bend liquid crystal phase of a flexible linear trimer and homologous dimer. Proceedings of the National Academy of Sciences. 2019;116(22):10698-10704.
14. Mandle RJ. A Ten-Year Perspective on Twist-Bend Nematic Materials. Molecules. 2022;27(9):2689.
15. McGlen RJ, Jachuck R, Lin S. Integrated thermal management techniques for high power electronic devices. Appl Therm Eng. 2004;24(8-9):1143-1156.
16. Han W, Qiu S, Chen J, Zhong X, Hao L, Chen H, et al. One-pot synthesis of mesoporous silica-supported nano-metal oxide composites with enhanced antibacterial properties. Materials Chemistry and Physics. 2022;290:126618.
17. Bijesh P, Selvaraj V, Andal V. A review on synthesis and applications of nano metal Oxide/porous carbon composite. Materials Today: Proceedings. 2022;55:212-219.
18. Qu J, Che N, Niu G, Liu L, Li C, Liu Y. Iron/manganese binary metal oxide-biochar nano-composites with high adsorption capacities of Cd2+: Preparation and adsorption mechanisms. Journal of Water Process Engineering. 2023;51:103332.
19. Chen Z, Li J, Wang S, Zhao J, Liu J, Shen J, et al. Structure-property-performance relationship of transition metal doped WO3 mixed oxides for catalytic degradation of organic pollutants. Chemosphere. 2023;316:137797.
20. Alavi M, Kamarasu P, McClements DJ, Moore MD. Metal and metal oxide-based antiviral nanoparticles: Properties, mechanisms of action, and applications. Advances in Colloid and Interface Science. 2022;306:102726.
21. Strachowski T, Baran M, Chlanda A, Grzanka E. Effect of annealing in argon atmosphere on the properties of zinc oxide nanoparticles doped with Mn(II) and Co(II) ions prepared in solvothermal synthesis. Ceram Int. 2022;48(17):24935-24942.
22. Alshammari FH. Physical characterization and dielectric properties of chitosan incorporated by zinc oxide and graphene oxide nanoparticles prepared via laser ablation route. Journal of Materials Research and Technology. 2022;20:740-747.
23. Nandanapalli KR, Mudusu D, Lingandhinne RMR, Lee SW. Passivation layer–dependent catalysis of zinc oxide nanostructures. Materials Today Chemistry.

2021;22:100592.
24. Zhao J, Chen L, Luo W, Li H, Wu Z, Xu Z, et al. Strong tribo-catalysis of zinc oxide nanorods via triboelectrically-harvesting friction energy. Ceram Int. 2020;46(16):25293-25298.
25. Sathishkumar P, Li Z, Govindan R, Jayakumar R, Wang C, Long Gu F. Zinc oxide-quercetin nanocomposite as a smart nano-drug delivery system: Molecular-level interaction studies. Appl Surf Sci. 2021;536:147741.
26. Stockey Erhardt C, Guaglianoni W, Garcia AP, Basegio TM, Bergmann CP. Ultra-rapid microwave-assisted synthesis of gallium doped zinc oxide for enhanced photocurrent generation. Ceram Int. 2023;49(8):12231-12239.
27. Dhanemozhi AC, Rajeswari V, Sathyajothi S. Green Synthesis of Zinc Oxide Nanoparticle Using Green Tea Leaf Extract for Supercapacitor Application. Materials Today: Proceedings. 2017;4(2):660-667.
28. Król A, Pomastowski P, Rafińska K, Railean-Plugaru V, Buszewski B. Zinc oxide nanoparticles: Synthesis, antiseptic activity and toxicity mechanism. Advances in Colloid and Interface Science. 2017;249:37-52.
29. Dutta S, Jaiswal KK, Verma R, Basavaraju DM, Ramaswamy AP. Green synthesis of zinc oxide catalyst under microwave irradiation using banana (Musa spp.) corm (rhizome) extract for biodiesel synthesis from fish waste lipid. Biocatalysis and Agricultural Biotechnology. 2019;22:101390.
30. Tabrizi Hafez Moghaddas SM, Elahi B, Darroudi M, Javanbakht V. Green synthesis of hexagonal-shaped zinc oxide nanosheets using mucilage from flaxseed for removal of methylene blue from aqueous solution. J Mol Liq. 2019;296:111834.
31. Happy A, Soumya M, Venkat Kumar S, Rajeshkumar S, Sheba RD, Lakshmi T, et al. Phyto-assisted synthesis of zinc oxide nanoparticles using Cassia alata and its antibacterial activity against Escherichia coli. Biochemistry and Biophysics Reports. 2019;17:208-211.
32. Singh TA, Das J, Sil PC. Zinc oxide nanoparticles: A comprehensive review on its synthesis, anticancer and drug delivery applications as well as health risks. Advances in Colloid and Interface Science. 2020;286:102317.
33. Kavitha A, Doss A, Praveen Pole RP, Pushpa Rani TPK, Prasad R, Satheesh S. A mini review on plant-mediated zinc oxide nanoparticles and their antibacterial potency. Biocatalysis and Agricultural Biotechnology. 2023;48:102654.
34. Cui Y, Tian Z, Lu H, Deng D, Liu Z, Rong T, et al. Zinc oxide nanoparticles improve gut health and reduce faecal zinc excretion in piglets. Livestock Science. 2021;251:104610.
35. Almansour MI, Alferah MA, Shraideh ZA, Jarrar BM. Zinc oxide nanoparticles hepatotoxicity: Histological and histochemical study. Environmental Toxicology and Pharmacology. 2017;51:124-130.
36. Kim K-B, Kim YW, Lim SK, Roh TH, Bang DY, Choi SM, et al. Risk assessment of zinc oxide, a cosmetic ingredient used as a UV filter of sunscreens. Journal of Toxicology and Environmental Health, Part B. 2017;20(3):155-182.
37. Saliba S, Coppel Y, Davidson P, Mingotaud C, Chaudret B, Kahn ML, et al. Liquid crystal based on hybrid zinc oxide nanoparticles. J Mater Chem. 2011;21(19):6821.
38. Elkhalgi HHM, Khandka S, Yadav N, Dhar R, Dabrowski R. Effects of manganese (II) titanium oxide nano particles on the physical properties of a room temperature nematic liquid crystal 4-(trans-4′-n-hexylcyclohexyl) isothiocyanatobenzene. J Mol Liq. 2018;268:223-228.
39. Kim DH, Lee DW, Oh JY, Won J, Seo D-S. Nanopatterning of Polymer/Gallium Oxide Thin Films by UV-Curing Nanoimprint Lithography for Liquid Crystal Alignment. ACS Applied Nano Materials. 2022;5(1):1435-1445.
40. Oriented Yttrium Strontium Tin Oxide Micro/Nanostructures Induced by Brush Coating for Low-Voltage Liquid Crystal Systems. American Chemical Society (ACS).
41. Mohammad A-T, H. T S, Alrawi RY. Isoflavone-based trimer liquid crystals: synthesis, characterization, thermal and mesomorphic properties evaluations. Liq Cryst. 2019;47(1):28-35.
42. I. Al-jobury A, S. Mohammed A, A. Al-badrany K. Synthesis of some new Pyrazoline derivatives derived from Ibuprofen. Kirkuk University Journal-Scientific Studies. 2016;11(3):254-262.
43. Aldujaili R, Alhasan A. Preparation and Characterization of some new Benzothiazole-Heterocyclic Derivatives. Egyptian Journal of Chemistry. 2021;64(6):8-9.
44. Fu Y, Liu D, Zeng H, Ren X, Song B, Hu D, et al. New chalcone derivatives: synthesis, antiviral activity and mechanism of action. RSC Advances. 2020;10(41):24483-24490.
45. Mohammad A-T, Mustafa HK. Unsymmetrical Coumarin based dimeric liquid crystals: Synthesis, Characterization, Mesomorphic investigation, Photoluminescence and Thermal conductivity. Liq Cryst. 2021;49(3):354-365.
46. Akhtar MN, Sakeh NM, Zareen S, Gul S, Lo KM, Ul-Haq Z, et al. Design and synthesis of chalcone derivatives as potent tyrosinase inhibitors and their structural activity relationship. J Mol Struct. 2015;1085:97-103.
47. Ha S-T, Koh T-M, Yeap G-Y, Lin H-C, Lee S-L, Win Y-F, et al. Synthesis and Mesomorphic Properties of 6-Methoxy- and 6-Ethoxy-2-(2-Hydroxy-4-Alkanoyloxybenzylidenamino) Benzothiazoles. Mol Cryst Liq Cryst. 2010;528(1):10-22.
48. Yeap G-Y, Hng T-C, Takeuchi D, Osakada K, Ahmad Kamil Mahmood W, Ito MM. Non-Symmetric Liquid Crystal Dimers: High Thermal Stability in Nematic Phase Enhanced by Thiophene-2-Carboxylate Moiety. Mol Cryst Liq Cryst. 2009;506(1):134-149.
49. Alam TM, Pearce CJ. Impact of graphene incorporation on the orientational order of graphene/liquid crystal composites. Chem Phys Lett. 2014;592:7-13.
50. Shen Y, Cong Yh, Zhang By, Lang Qy. The Side-Chain Liquid Crystalline Epoxy Polymer Grafted Nanoparticles for the Thermal and Mechanical Enhancement of Epoxy Nanocomposites. ChemistrySelect. 2019;4(27):8104-8111.
51. Fakhri FH, Ahmed LM. Incorporation CdS with ZnS as Composite and Using in Photo-Decolorization of Congo Red Dye. Indonesian Journal of Chemistry. 2019;19(4):936.
52. Ahmed L, S. Fadhil E, F. Mohammed A. Effect of silver doping on structural and photocatalytic circumstances of ZnO nanoparticles. Iraqi Journal of Nanotechnology. 2020(1):13-20.
53. N AT, Adhikari AV. 2-Methoxypyridine derivatives: synthesis, liquid crystalline and photo-physical properties. New J Chem. 2014;38(10):5018-5029.
54. Jebapriya JC, Jonathan DR, Kirupavathy SS, Ragu R, Prasana JC. Growth and characterization of a cyclohexanone based chalcone crystal 2(E)-(4-N,N-dimethylaminobenzylidene)-5-methylcyclohexanone for nonlinear optical applications. Opt Mater. 2020;107:110035.
55. Bonifácio VDB, Correia VG, Pinho MG, Lima JC, Aguiar-Ricardo A. Blue emission of carbamic acid oligooxazoline biotags. Mater Lett. 2012;81:205-208.